

**Dehydration of fatty alcohols on zirconia supported tungstate catalysts**

Journal:	<i>Catalysis Science &amp; Technology</i>
Manuscript ID	CY-ART-04-2022-000785.R3
Article Type:	Paper
Date Submitted by the Author:	29-Aug-2022
Complete List of Authors:	Milakovic, Lara; Technische Universität München Fakultät für Chemie Liu, Yue; Technische Universität München, Barath, Eszter; Leibniz-Institut für Katalyse eV, Lercher, Johannes; Technische Universität München Physik-Department,

## ARTICLE

## Dehydration of fatty alcohols on zirconia supported tungstate catalysts

Lara Milaković,<sup>a</sup> Yue Liu,<sup>a</sup> Eszter Baráth,<sup>\*a,b</sup> and Johannes A. Lercher<sup>\*a,c</sup>

Received 00th January 20xx,  
Accepted 00th January 20xx

DOI: 10.1039/x0xx00000x

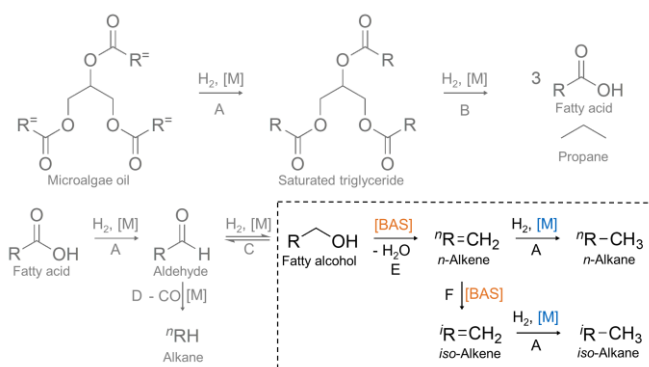
Zirconia supported tungstates catalyze octadecanol dehydration, an important step in the carbon preserving conversion of triglycerides to fuels. This study shows the dependence of the tetragonal zirconia phase of  $\text{WO}_3/\text{ZrO}_2$  on the formation of Zr-stabilized  $\text{WO}_3$  clusters, leading to the highest Brønsted acid site concentrations and in turn to the highest octadecanol dehydration rates. Small concentrations of Pt increased the Brønsted acid site concentrations by stabilizing partly reduced tungstates.

### Introduction

Since Hino and Arata discovered the hydrothermally stable  $\text{WO}_3/\text{ZrO}_2$  as a strong solid acid catalyst, considerable interest was raised in its catalytic properties.<sup>1</sup> Extensive research has been conducted employing tungstated zirconia as catalyst for various reactions such as isomerization of light alkanes,<sup>1-3</sup> selective catalytic reduction of  $\text{NO}_x$ ,<sup>4</sup> and dehydration of alcohols.<sup>5-7</sup> In general, the tungsten surface density is presumed to be the key indicator for the catalytic activity. There is a general agreement on the differentiation between four tungsten surface species.<sup>3, 7-11</sup> In sub-monolayer concentrations octahedral isolated mono-oxo  $\text{W}=\text{O}$  species grow with increasing W surface density to polymeric mono-oxo  $\text{W}=\text{O}$  species. After reaching monolayer surface coverage, crystalline, monoclinic  $\text{WO}_3$  nanoparticles start to form.<sup>7, 12</sup> Under certain conditions these Zr-stabilized  $\text{WO}_3$  nanoparticles can co-exist with monomeric and polymeric  $\text{W}=\text{O}$  containing species.<sup>7-9</sup>

Our recent study, moreover, revealed the significant influence of the tungstate support.<sup>13</sup> The aqueous phase dehydration of cyclohexanol showed a drastically increase of the turnover frequency for the activated carbon support induced by changes of the local ionic strength and in turn the excess chemical potential. Besides, differences between two polymorphs of the zirconia support were indicated, which has also been previously addressed.<sup>7, 14</sup> However, there are still discrepancies regarding the source of the catalytic activity.<sup>3, 7, 14-17</sup> For instance, while Lebarbier et al.<sup>14</sup> attribute the different activity of the two polymorphs mainly to the crystalline composition (tetragonal vs. monoclinic zirconia), Ross-Medgaarden et al.<sup>7</sup> reason that the catalytic differences are primarily based on the presence of Zr-stabilized  $\text{WO}_3$  nanoparticles.

In this study, we investigate the origin of the surface differences of the zirconia support by examining the fatty alcohol dehydration (highlighted in Scheme 1) with octadecanol as the model compound on two different zirconia supported tungstate catalysts and additional platinum promotion in organic phase. Dehydration of fatty alcohols is an important step in the hydrodeoxygenation of microalgae oil to hydrocarbon fuel which is considered an important alternative to petroleum-based fuels due to the promising properties of microalgae such as their high abundance and rapid growth.<sup>18, 19</sup> The fatty acids of microalgae oil consist typically of a chain length between 14 – 22 carbon atoms.<sup>19, 20</sup> Thus, their hydrodeoxygenation produces diesel-like transportation fuel.<sup>19, 21, 22</sup> In recent years, the further conversion to hydrocarbons in the kerosene range for utilization in the aviation sector has attracted increasing interest.<sup>23</sup> This can be implemented by incorporating additionally a hydroisomerization or -cracking step. The reaction mechanism of the hydrodeoxygenation of microalgae oil to hydrocarbon fuel with a bifunctional catalyst is depicted in Scheme 1. The first step is the metal ([M]) catalyzed hydrogenation (A) of the unsaturated bonds in the triglyceride, followed by hydrogenolysis (B) to fatty acids and propane.



**Scheme 1** Reaction mechanism of the microalgae oil hydrodeoxygenation to hydrocarbon fuel with a bifunctional catalyst, and highlighted the fatty alcohol dehydration. A = hydrogenation, B = hydrogenolysis, C = (de-)hydrogenation, D = decarbonylation, E = dehydration, F = isomerization.

<sup>a</sup> Technische Universität München, Department of Chemistry and Catalysis Research Center, Lichtenbergstraße 4, 85748 Garching, Germany.

E-mail: eszter.barath@catalysis.de, johannes.lercher@ch.tum.de

<sup>b</sup> Current address: Leibniz-Institut für Katalyse e.V. (LIKAT Rostock), Albert-Einstein-Str. 29a, 18059 Rostock, Germany

<sup>c</sup> Institute for Integrated Catalysis, Pacific Northwest National Laboratory, 902 Battelle Boulevard, Richland, WA 99352, USA.

† Electronic Supplementary Information (ESI) available: See DOI: 10.1039/x0xx00000x

The fatty acid is then hydrogenated (A) to an aldehyde which is in equilibrium with the corresponding fatty alcohol (C) or can undergo decarbonylation (D) to a *n*-alkane.

In the presence of Brønsted acid sites (BAS), the fatty alcohol is dehydrated (E) to a *n*-alkene. This is in turn either isomerized (F) and then further hydrogenated (A) to an *iso*-alkane or is just directly hydrogenated (A) to the saturated and unbranched *n*-alkane.<sup>21</sup> As the microalgae are cultivated in an aqueous environment, the zirconia supported tungstate catalysts fulfill the requirement of being stable in water and at the same time provide the needed Brønsted acidity.<sup>1</sup>

## Results and discussion

### Characterization

WO<sub>3</sub>/ZrO<sub>2</sub> catalysts with different tungsten oxide loading in the range between 5.9 to 27.4 wt.% were synthesized via two methods. One method incorporated the WO<sub>3</sub> onto a pre-calcined crystalline zirconia (ZrO<sub>2</sub>) support (subsequently referred to as xWZrO<sub>2</sub>(y), with x indicating the WO<sub>3</sub> loading and y the W surface density), while for the other an incipient wetness impregnation directly onto the amorphous zirconium hydroxide (Zr(OH)<sub>4</sub>) was conducted (xWZrOH(y)). Further details of the synthesis can be found in the Experimental section.

The physicochemical properties of the investigated catalyst are summarized in Table 1. The tungsten surface density is calculated based on the WO<sub>3</sub> loadings and the specific surface areas (detailed calculation in the Experimental section).<sup>7</sup> As the surface area depends on the calcination temperature, it also influences the WO<sub>x</sub> surface density.<sup>7, 24</sup> This study uses a pre-calcination temperature of 800°C. While the W surface density increased expectedly with increasing W loadings (Table 1, ESI,† Fig. S1), the specific surface areas of the final materials passed through a maximum. The increase of the BET surface area is attributed to stabilization of the zirconia support by direct interaction with the octahedral tungstates via covalent W-O-Zr bonds<sup>7</sup> that block nucleation sites, reduce surface diffusivity and inhibit so sintering of the ZrO<sub>2</sub> support.<sup>16, 24, 25</sup> The specific surface area decreased once the monolayer coverage was reached.<sup>26</sup> Using the maximum as indication, a W surface density above 4.6 and 4.0 W nm<sup>-2</sup> for the WZrO<sub>2</sub> and WZrOH catalysts was considered to be monolayer coverage.<sup>7, 12, 27-30</sup> In general, the WZrOH catalysts showed higher BET surface areas than the WZrO<sub>2</sub> catalysts, which is attributed to the more facile surface stabilization in presence of the higher concentration of hydroxyl groups to develop W-O-Zr bonds.

In order to better understand the surface composition of the catalysts Raman spectroscopy was used. The Raman spectra of the WZrO<sub>2</sub> are presented in Fig. 1 A. Most bands below 700 cm<sup>-1</sup> are attributed to monoclinic ZrO<sub>2</sub> with bands at 180, 192, 220, 308, 335, 349, 383, 476, 503, 539, 561, 617, and 638 cm<sup>-1</sup>.<sup>7, 31</sup>

**Table 1** Physicochemical properties of the studied WZrO<sub>2</sub> and WZrOH catalysts.

WZrO <sub>2</sub>	BET surface area (m <sup>2</sup> g <sup>-1</sup> )	W surface density (W nm <sup>-2</sup> ) <sup>a</sup>	c (BAS) (mmol g <sup>-1</sup> ) <sup>b</sup>	WZrOH	BET surface area (m <sup>2</sup> g <sup>-1</sup> )	W surface density (W nm <sup>-2</sup> ) <sup>a</sup>	c (BAS) (mmol g <sup>-1</sup> ) <sup>b</sup>
7.3 wt.% WO <sub>3</sub> /ZrO <sub>2</sub>	66	2.8	0.008	5.9 wt.% WO <sub>3</sub> /ZrO <sub>2</sub>	63	2.4	0.004
12.2 wt.% WO <sub>3</sub> /ZrO <sub>2</sub>	70	4.6	0.015	10.3 wt.% WO <sub>3</sub> /ZrO <sub>2</sub>	71	3.7	0.023
14.6 wt.% WO <sub>3</sub> /ZrO <sub>2</sub>	66	5.7	0.019	13.8 wt.% WO <sub>3</sub> /ZrO <sub>2</sub>	91	4.0	0.033
17.4 wt.% WO <sub>3</sub> /ZrO <sub>2</sub>	64	7.1	0.023	14.9 wt.% WO <sub>3</sub> /ZrO <sub>2</sub>	87	4.5	0.035
19.4 wt.% WO <sub>3</sub> /ZrO <sub>2</sub>	60	8.5	0.022	16.2 wt.% WO <sub>3</sub> /ZrO <sub>2</sub>	78	5.4	0.038
22.0 wt.% WO <sub>3</sub> /ZrO <sub>2</sub>	53	10.9	0.020	18.2 wt.% WO <sub>3</sub> /ZrO <sub>2</sub>	77	6.2	0.035
24.4 wt.% WO <sub>3</sub> /ZrO <sub>2</sub>	49	13.0	0.016	20.6 wt.% WO <sub>3</sub> /ZrO <sub>2</sub>	63	8.6	0.029
27.4 wt.% WO <sub>3</sub> /ZrO <sub>2</sub>	44	16.1	0.011	24.8 wt.% WO <sub>3</sub> /ZrO <sub>2</sub>	60	10.7	0.018

<sup>a</sup>Detailed calculation in the Experimental section. <sup>b</sup>Determined from IR spectroscopy of adsorbed pyridine.

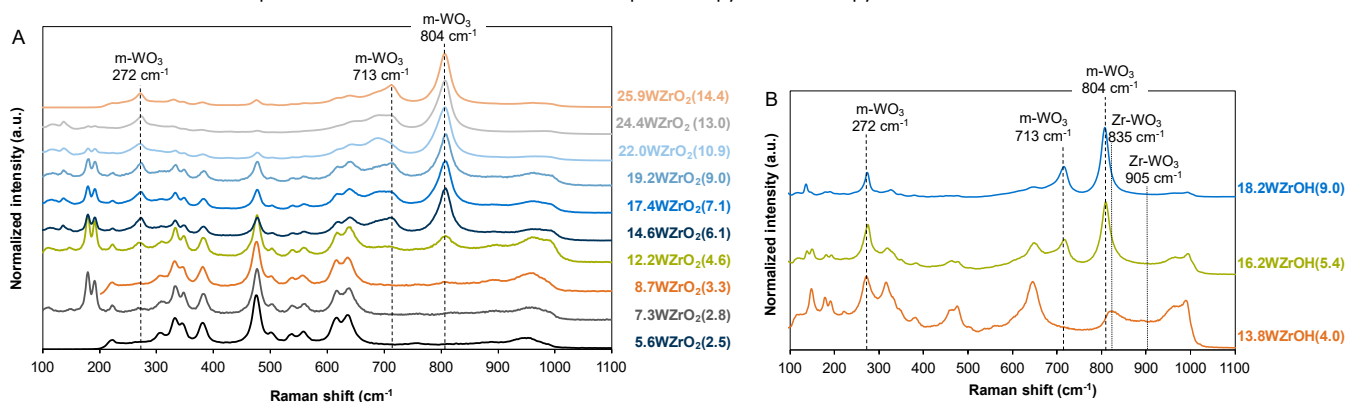


**Fig. 1** Raman shift of the WZrO<sub>2</sub> (A) and WZrOH (B) catalysts with different WO<sub>3</sub> loadings with identification of the characteristic bands of m-WO<sub>3</sub> and Zr-WO<sub>3</sub>.

## ARTICLE

The intensity of these bands, however, decreased with increasing tungsten coverage. Above a W surface density of  $4.6 \text{ W nm}^{-2}$  the characteristic bands of crystalline m-WO<sub>3</sub> at 272, 713, and  $804 \text{ cm}^{-1}$  were detected.<sup>12, 14, 28, 30</sup> The broad bands around  $960 - 970 \text{ cm}^{-1}$  are attributed to isolated mono-oxo W=O species, shifting toward  $1000 \text{ cm}^{-1}$  when polymeric mono-oxo W=O species evolve with increasing tungsten loading.<sup>12, 14, 28, 30</sup>

On WZrOH catalysts (Fig. 1 B), the appearance of characteristic bands of crystalline m-WO<sub>3</sub> ( $272, 713, \text{ and } 804 \text{ cm}^{-1}$ ) suggest that monolayer coverage is reached above  $4.0 \text{ W nm}^{-2}$ . Below  $700 \text{ cm}^{-1}$  mainly bands of t-ZrO<sub>2</sub> at 149, 319, 464, 476, and  $647 \text{ cm}^{-1}$  were detected, which were also decreasing with higher W surface density.<sup>7, 31</sup> As these bands partly overlap with those of monoclinic ZrO<sub>2</sub> the phase composition was additionally probed by XRD. Further, also bands of isolated and polymeric mono-oxo W=O species are presented around  $960 - 970 \text{ cm}^{-1}$  and  $1000 \text{ cm}^{-1}$ , respectively.<sup>12, 14, 28, 30</sup> The 13.8WZrOH(4.0) catalyst showed additional bands at  $835 \text{ cm}^{-1}$  and a wider less intense at  $905 \text{ cm}^{-1}$ , assigned to three-dimensional distorted Zr-WO<sub>3</sub> clusters.<sup>8</sup> As their characteristic band ( $835 \text{ cm}^{-1}$ ) overlaps with the strong band of m-WO<sub>3</sub> ( $804 \text{ cm}^{-1}$ ), it can only be hypothesized that the Zr-stabilized WO<sub>3</sub> clusters are also present in the other catalysts. Due to the fact that Raman-spectroscopy is not perfectly suited for the identification of the Zr-WO<sub>3</sub> species above monolayer coverage, their existence has not been experimentally observed. In 2009, however, Zhou et al. provided direct imaging of this species with the help of high-angle annular dark-field imaging in an aberration-corrected STEM.<sup>8</sup>

At high temperature pure zirconia is transformed from the metastable tetragonal to the thermodynamically stable

monoclinic phase.<sup>32</sup> This transformation is retarded by the stabilizing interaction with the tungstates.<sup>24, 25</sup> Table 2 summarizes the fractions of these two phases determined by X-ray diffraction (all XRD patterns in ESI, † Fig. S2 and S3).

Fig. 2 assigns the reflections of the XRD patterns of the 17.4WZrO<sub>2</sub>(7.1), 16.2WZrOH(5.4), and 0.5Pt16.2WZrOH(5.4) catalysts to either monoclinic or tetragonal phases. The WZrO<sub>2</sub> catalysts have a significantly higher fraction of m-ZrO<sub>2</sub> than the WZrOH catalysts, because of the lack of stabilization by tungstates during the pre-calcination of the zirconia support at  $400^\circ\text{C}$ , where the t-ZrO<sub>2</sub> was already partly transformed.

The 0.5Pt16.2WZrOH(5.4) catalyst on the contrary, only suffers a minor loss of the tetragonal phase despite the repeated thermal treatment. With increasing WO<sub>3</sub> loading, the fraction of t-ZrO<sub>2</sub> is growing and levels off at high loadings. It is interesting to note that this decrease occurs, in contrast to the BET surface area, above monolayer coverage.

The Brønsted acid site concentration of the catalysts, which is summarized in Table 1, is presented as a function of the tungsten loading in Fig. 3. It is shown that the BAS concentration

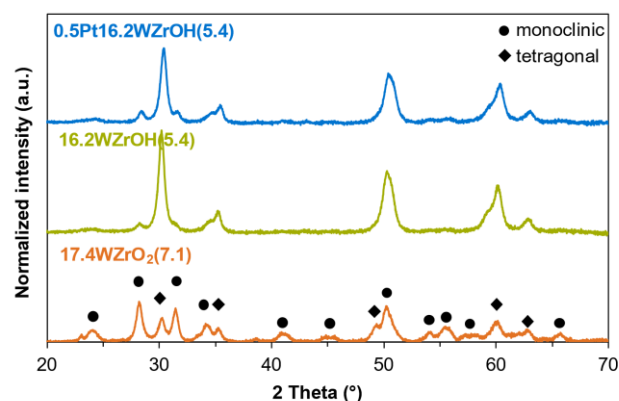


Fig. 2 patterns of a WZrO<sub>2</sub>, WZrOH and PtWZrOH catalyst with the assignment of the reflections to the monoclinic or tetragonal phase

Table 2 Content of the monoclinic or tetragonal phase in the WZrO<sub>2</sub> and WZrOH catalysts derived from XRD.

WZrO <sub>2</sub>	m-ZrO <sub>2</sub> (%)	t-ZrO <sub>2</sub> (%)	WZrOH	m-ZrO <sub>2</sub> (%)	t-ZrO <sub>2</sub> (%)
ZrO <sub>2</sub> (400°C)	63	37	5.9 wt.% WO <sub>3</sub> /ZrO <sub>2</sub>	73	28
ZrO <sub>2</sub> (800°C)	92	8	10.3 wt.% WO <sub>3</sub> /ZrO <sub>2</sub>	54	46
5.6 wt.% WO <sub>3</sub> /ZrO <sub>2</sub>	90	10	12.5 wt.% WO <sub>3</sub> /ZrO <sub>2</sub>	41	59
8.7 wt.% WO <sub>3</sub> /ZrO <sub>2</sub>	88	12	14.9 wt.% WO <sub>3</sub> /ZrO <sub>2</sub>	25	75
12.2 wt.% WO <sub>3</sub> /ZrO <sub>2</sub>	85	15	16.2 wt.% WO <sub>3</sub> /ZrO <sub>2</sub>	23	77
17.4 wt.% WO <sub>3</sub> /ZrO <sub>2</sub>	81	19	18.2 wt.% WO <sub>3</sub> /ZrO <sub>2</sub>	26	74
22.0 wt.% WO <sub>3</sub> /ZrO <sub>2</sub>	84	16	0.5 wt.% Pt 16.2 wt.% WO <sub>3</sub> /ZrO <sub>2</sub>	33	67

## ARTICLE

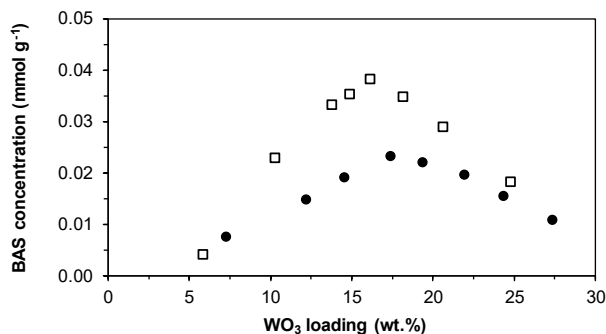


Fig. 3 BAS concentrations as function of the WO<sub>3</sub> loading of different WZrO<sub>2</sub> (●) and WZrOH (□) catalysts.

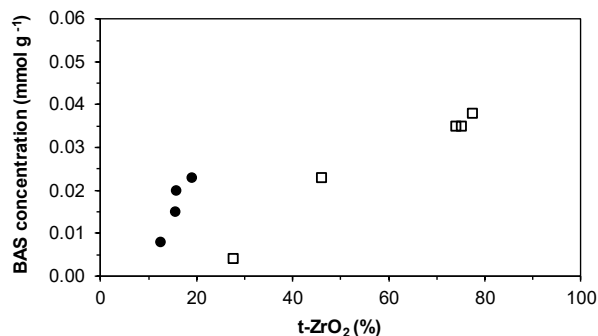


Fig. 4 Correlation of the BAS concentration and the fraction of the tetragonal phase for both WZrO<sub>2</sub> (●) and WZrOH (□) catalysts.

passes through a maximum by increasing the tungsten loading (analogous dependency of BAS concentration by increasing the W surface density, ESI,† Fig. S4). As BAS can originate from acidic hydroxyl groups associated with W-O-W and W-O-Zr bonds, an increase of the tungsten loading, and in turn the W surface density, will result in a higher concentration of these bonds and, therefore, a higher concentration of Brønsted acid sites.<sup>33</sup> In other words, by increasing the tungstate domain size the associated ability of the conjugate base to delocalize electrons upon deprotonation of the acid is increased.<sup>9</sup> However, with increasing tungsten loading large crystalline WO<sub>3</sub> particles start to form. Therefore, more and more W centers become inaccessible which results in a decrease of the BAS concentration.<sup>12</sup> It should be noted in passing that when discussing the dependency of the W surface density on the BAS concentration, the impact of the surface area is also being taken into account as these two parameters are interdependent.

The highest concentrations were observed above monolayer coverage on the 17.4WZrO<sub>2</sub>(7.1) and 16.2WZrOH(5.4) catalyst with 0.023 and 0.038 mmol g<sup>-1</sup>, respectively, which is in line with the highest fraction of t-ZrO<sub>2</sub>. Thus, the BAS concentration continues to increase, even after crystalline WO<sub>3</sub> particles are formed. This indicates that an additional species could exist, namely Zr-stabilized WO<sub>3</sub> nanoparticles, which contribute to the acidity of the catalysts. In literature it is speculated that Zr-stabilized WO<sub>3</sub> nanoparticles are the most active species.<sup>7, 8</sup> In line, density functional theory calculations of the Brønsted acidity of these Zr-WO<sub>3</sub> nanoparticles have shown that they have the lowest deprotonation energy.<sup>9, 34</sup>

Remarkably, the BAS concentration correlates positively with the fraction of t-ZrO<sub>2</sub> (Fig. 4). While the origin of this correlation needs further investigations, empirically it explains the significantly higher BAS concentrations in WZrOH compared to WZrO<sub>2</sub> catalysts. The BAS concentration, which is maximized by increasing the concentration of Zr-WO<sub>3</sub> clusters, has, therefore,

a direct relation with the tetragonal phase of the zirconia support.

It is assumed that the clusters can only be formed on the t-ZrO<sub>2</sub>. This could be due to their different lattice structures. While the monoclinic polymorph has heptacoordinated Zr<sup>4+</sup> cations and either tri- or tetraordinated O<sup>2-</sup> anions, the lattice of tetragonal zirconia consists of octacoordinated Zr<sup>4+</sup> cations and exclusively of tetraordinated O<sup>2-</sup> anions.<sup>35</sup> Recognizing that the presence of Zr-stabilized WO<sub>3</sub> nanoparticles and the tetragonal zirconia phase are interdependent, also harmonizes some conflicts in literature where it was believed that predominantly only one of these parameters is the main source of the catalytic activity.<sup>3, 7, 14-17</sup>

#### Octadecanol dehydration

The time-dependent conversion of octadecanol in a batch reactor with 17.4WZrO<sub>2</sub>(7.1) and 16.2WZrOH(5.4) are shown in Fig. 5 A and B, respectively. With both catalysts *iso*-octadecene was selectively formed. Small amounts of *n*-octadecene and octadecanal were detected. The reaction order in the alcohol was zero (ESI,† Fig. S5). After 240 min around 77% of octadecanol were converted with 17.4WZrO<sub>2</sub>(7.1) catalyst, 83% with 16.2WZrOH(5.4) catalyst already after 60 min reaction time. This superior catalytic activity of the zirconium hydroxide based catalyst is also demonstrated in Fig. 5 C, in which octadecanol dehydration rates are plotted versus the WO<sub>3</sub> loading for both series of catalysts. At equal tungstate concentrations, WZrO<sub>2</sub> (●) catalysts had an almost three-fold lower rate than the corresponding WZrOH (□) catalysts. The highest rate within a series was observed on 17.4WZrO<sub>2</sub>(7.1) catalyst with 2.0 × 10<sup>-6</sup> mol g<sup>-1</sup> s<sup>-1</sup> and on 16.2WZrOH(5.4) with 5.2 × 10<sup>-6</sup> mol g<sup>-1</sup> s<sup>-1</sup>. The rates show a volcano-shaped dependency on the WO<sub>3</sub> loading and on the tungstate surface density which also parallels the BAS concentrations (Fig. 3 and 5 C, ESI,† Fig. S4 and S6), coinciding to the hypothesis of the

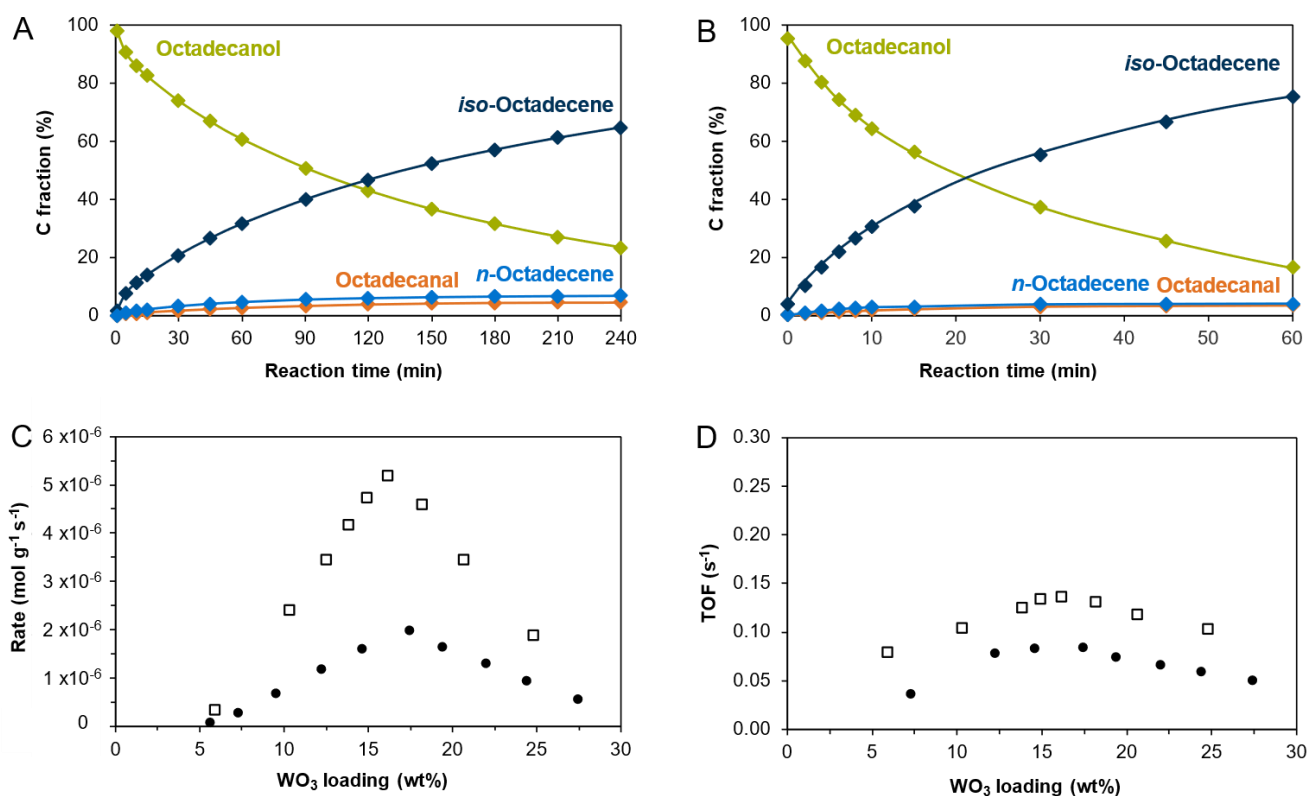


**Fig. 5** Product distribution of the octadecanol dehydration with 17.4WZrO<sub>2</sub>(7.1) (A) and 16.2WZrOH(5.4) (B) catalysts. Rate (C) and TOF (D) of the octadecanol dehydration as function of the WO<sub>3</sub> loading on different WZrO<sub>2</sub> (●) and WZrOH (□) catalysts. Reaction conditions: catalyst (0.2 g), octadecanol (0.5 g), decalin (100 mL), 180°C,  $p(\text{H}_2) = 40$  bar, 700 rpm.

presence of Zr-stabilized WO<sub>3</sub> nanoparticles as the most active species. From a practical point it appears, therefore, that the highest activity is achieved with amorphous zirconium hydroxide support loaded with a medium W surface density.<sup>3, 5, 6, 9, 10</sup>

Analyzing the turnover frequency (TOF), by normalizing the weight-based rate by the BAS concentration, it would be expected to see a constant dependency of the TOF on the tungsten loading. Fig. 5 D shows a slight increase of the TOF for medium tungsten loadings (also for medium W surface densities, ESI,† Fig. S7). Therefore, further investigations are necessary to differentiate between the strength of the acid sites of the Zr-WO<sub>3</sub> nanoparticles which cause this deviation in TOF plot. The activation energy is rather constant throughout the varying WO<sub>3</sub> content, however, is more than twice as high for the WZrO<sub>2</sub> catalysts in comparison to the WZrOH (e.g., ESI,† 14.6WZrO<sub>2</sub>(5.6): 97 kJ mol<sup>-1</sup> vs. 14.9WZrOH(4.5): 38 kJ mol<sup>-1</sup>, Fig. S8).

#### Promotion effect of platinum

As the conversion of triglycerides requires bifunctional, metal containing catalysts, the impact of Pt on the WZrOH catalysts was explored for dehydration. In order to exclude dehydration activity of the platinum, octadecanol was tested with a non-acidic Pt on carbon catalyst, which showed no conversion. Additionally, the results from our previous studies, investigating the HDO reaction network of long chain fatty acids with Ni on SiO<sub>2</sub> and ZrO<sub>2</sub>, support this hypothesis.<sup>36-38</sup>

Fig. 6 A shows that the main product of the conversion over the 0.5Pt16.2WZrOH(5.4) catalyst was (expectedly) *n*-octadecane, while only small amounts of *iso*-octadecane and traces of octadecanol were detected. This allows to conclude that the hydrogenation rate was higher under the explored experimental conditions compared to the isomerization rate. Additionally, the pressure and the relatively low reaction temperature led to a low concentration of alkenes and, hence, to a very low rate of hydroisomerization. Indeed, experiments with a constant total pressure but varying H<sub>2</sub> partial pressure showed that lower H<sub>2</sub> pressures led to a higher *iso*-octadecane formation rate, while the dehydration rate was unchanged (ESI,† Fig. S9). The rate of dehydration was also unaffected by varying the total pressure (ESI,† Fig. S10). The reaction order was determined to be zero in the alcohol (ESI,† Fig. S11). The weight normalized dehydration rate was as well independent of the carbon chain length of the converted substrate (C15 – C18, ESI,† Fig. S12).

Also for the 0.5PtWZrOH (◆) catalysts a volcano-shaped rate dependency on the WO<sub>3</sub> loading was found (Fig. 6 B). The highest dehydration rate was measured with the catalyst having the same tungsten density as on the one without Pt. Although Pt is not actively participating in the dehydration reaction, the dehydration rates were enhanced by 40% up to 70% in presence of Pt (e.g., 5.2 × 10<sup>-6</sup> mol g<sup>-1</sup> s<sup>-1</sup> without Pt increased to 8.8 × 10<sup>-6</sup> mol g<sup>-1</sup> s<sup>-1</sup> with 0.5Pt16.2WZrOH(5.4)). The same was observed for 0.5PtWZrO<sub>2</sub> catalysts (ESI,† Note S1). It is hypothesized and has previously been reported that Pt in the presence of H<sub>2</sub>

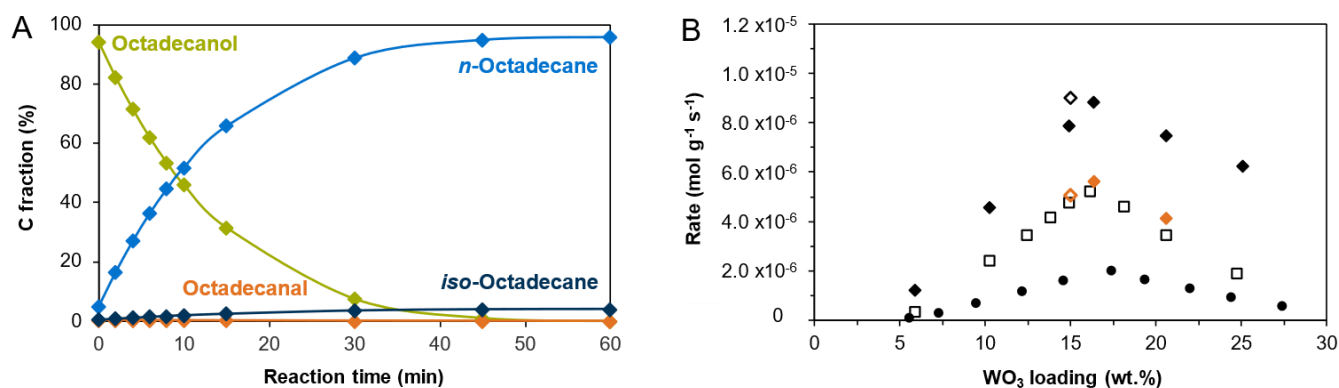


**Fig. 6** (A) Product distribution of the octadecanol dehydration over the 0.5Pt16.2WZrOH(5.4) catalyst. (B) Rate of the octadecanol dehydration as function of the WO<sub>3</sub> loading on different WZrO<sub>2</sub> (●), WZrOH (□), 0.5PtWZrOH (◆) and 1.5PtWZrOH (◇) catalysts in H<sub>2</sub>; and marked in orange in N<sub>2</sub>. Reaction conditions: catalyst (0.1 g), octadecanol (0.5 g), decalin (100 mL), 180°C,  $p(\text{H}_2/\text{N}_2) = 40$  bar, 700 rpm.

enables a partial reduction of the tungstates increasing the concentration of Brønsted acid sites (ESI,† Scheme S1).<sup>16, 26</sup> Indeed, when the reaction was conducted in N<sub>2</sub>, the rates were identical in presence and absence of Pt (marked in orange, Fig. 6 B). Expectedly, the product distribution of the Pt containing catalysts reverted to *iso*-octadecane as main product (ESI,† Fig. S13). Moreover, Fig. 6 B shows that increasing the amount of platinum to 1.5 wt.% (◇) slightly enhances the rate further. When conducting the reactions in nitrogen, this promotion again disappears (e.g., 14.9WZrOH(4.5): 4.7 x 10<sup>-6</sup> mol g<sup>-1</sup> s<sup>-1</sup>, 0.5Pt14.9WZrOH(4.5): 7.8 x 10<sup>-6</sup> mol g<sup>-1</sup> s<sup>-1</sup>, 1.5Pt14.9WZrOH(4.5): 9.0 x 10<sup>-6</sup> mol g<sup>-1</sup> s<sup>-1</sup> (H<sub>2</sub>), 5.0 x 10<sup>-6</sup> mol g<sup>-1</sup> s<sup>-1</sup> (N<sub>2</sub>)). In general, the dehydration rate was increasing with an increasing Pt loading, while the *iso*-octadecane formation rate was decreasing (ESI,† Fig. S14).

## Conclusions

The octadecanol dehydration over WO<sub>3</sub> supported zirconia catalysts showed on volcano-shaped rate dependency on the tungsten loading independent of the initial crystallinity of the support (crystalline zirconia or amorphous zirconium hydroxide) or a metal promotion (with or without Pt). The maximum was consistently found above monolayer coverage, confirming the presence of a most active species.

Even though, Raman spectroscopy could only detect the presence of Zr-stabilized WO<sub>3</sub> clusters on the 13.8WZrOH(4.0) catalyst, following the evidence and conclusions of the work of Zhou et al.<sup>8</sup> in analogy to our results, it is hypothesized that Zr-WO<sub>3</sub> clusters as the most active species also exist on the other investigated catalysts.

Further, XRD measurements revealed the dependency of the occurrence of Zr-stabilized WO<sub>3</sub> clusters on the tetragonal zirconia phase. By maximizing this polymorph, the highest BAS concentrations were generated and in turn the highest octadecanol dehydration rates were obtained. During the pre-calcination of the crystalline zirconia support, t-ZrO<sub>2</sub> was already partly transformed to the monoclinic phase due to the absence of stabilizing interactions with the tungstates.

Consequently, the WZrO<sub>2</sub> catalysts had a lower activity than the WZrOH catalysts.

Incorporating platinum onto the WZrOH catalysts resulted in a rate enhancement, even though it is not involved in the reaction and has a similar t-WZrO<sub>2</sub> content as the sole WZrOH catalyst. The enhancement was presumably caused by a Pt facilitated reduction of the tungstates already at moderate temperatures in the presence of hydrogen.

## Experimental

### Chemicals

All chemicals were purchased commercially and were not further purified. The following chemicals were used: Nitrogen 5.0, hydrogen 5.0 and synthetic air (20.5 vol% oxygen, 79.5 vol% nitrogen) were obtained from *Westfalen*. Zr(OH)<sub>4</sub>·xH<sub>2</sub>O (XZO880/01) was supplied by *MEL Chemicals*. (NH<sub>4</sub>)<sub>6</sub>H<sub>2</sub>W<sub>12</sub>O<sub>40</sub>·xH<sub>2</sub>O (99.99% trace metals basis), Pt(NH<sub>3</sub>)<sub>4</sub>(NO<sub>3</sub>)<sub>2</sub> (99.995% trace metals basis), 1-octadecanol (*ReagentPlus*, 99%), 1-heptadecanol (98%), 1-hexadecanol (*ReagentPlus*, 99%) and 1-pentadecanol (99%) were acquired from *Sigma-Aldrich*. Decahydronaphthalene (mixture of *cis*- and *trans* isomers, ≥99.0%, for synthesis) was purchased from *Merck*.

### Catalyst preparation

**WO<sub>3</sub>/ZrO<sub>2</sub>:** For the synthesis of the WZrO<sub>2</sub> catalysts, the zirconium hydroxide was pre-calcined in synthetic air (flow rate: 100 mL min<sup>-1</sup>) at 400°C for 4 h (heating rate: 10°C min<sup>-1</sup>). The (NH<sub>4</sub>)<sub>6</sub>H<sub>2</sub>W<sub>12</sub>O<sub>40</sub>·xH<sub>2</sub>O precursor solution was added dropwise onto the ZrO<sub>2</sub> (WZrO<sub>2</sub>) or Zr(OH)<sub>4</sub>·xH<sub>2</sub>O (WZrOH) support by incipient wetness impregnation, dried over night at 110°C, and subsequently calcined in synthetic air (flow rate: 100 mL min<sup>-1</sup>) at 800°C for 3 h (heating rate: 10°C min<sup>-1</sup> until 700°C, afterwards 5°C min<sup>-1</sup>).

**Pt/WO<sub>3</sub>/ZrO<sub>2</sub>:** Platinum was incorporated onto the WZrOH catalysts also by incipient wetness impregnation with the tetraammineplatinum(II) nitrate precursor solution. The catalyst was thermally treated in N<sub>2</sub> (flow rate: 100 mL min<sup>-1</sup>) at

400°C for 3 h (heating rate: 3°C min<sup>-1</sup>) and then reduced in H<sub>2</sub> (flow rate: 100 mL min<sup>-1</sup>) at 400°C for 3 h (heating rate: 3°C min<sup>-1</sup>).

### Analysis Methods

**Elemental analysis:** The tungsten and platinum content was determined photometrically using a *Shimadzu UV-160* UV-VIS-NIR spectrometer. 25 mg of the tungsten sample was prepared by an alkaline pulping and analyzed by the absorbance of a trithiocyanatotungsten(V)-complex at 405 nm, while for the determination of the platinum content 100 mg of the sample were prepared by an acidic pulping and subsequently measured by the absorbance of a trichlorostannatoplatinum-complex at 403 nm.

**N<sub>2</sub> physisorption:** The specific surface area of the catalysts was determined by using a *Thermo Fisher Scientific Sorptomatic 1990 series* instrument. First, 150 mg of sample were outgassed at 300°C for two hours at 1.3 × 10<sup>-5</sup> bar. The adsorption-desorption isotherms were collected at -196°C in a N<sub>2</sub> pressure range from 0.9613 to 0.9626 bar. The specific surface areas were calculated by means of *Brunauer-Emmett-Teller* (BET) theory.

**Tungsten surface density:** The W surface densities were determined by the following equation adapted from Ross-Medgaarden et al.<sup>7</sup>:

$$W \text{ surface density } \left[ \frac{W}{nm^2} \right] = \frac{\left( \frac{WO_3 \text{ loading [wt. \%]}}{100} \right) \cdot N_A \left[ \frac{1}{mol} \right]}{M_{WO_3} \left[ \frac{g}{mol} \right] \cdot BET \text{ surface area } \left[ \frac{m^2}{g} \right] \cdot 10^{18}}$$

where  $N_A$  is the Avogadro constant and  $M_{WO_3}$  represents the molar mass of tungsten trioxide.

**IR spectra of adsorbed pyridine (Py-IR):** The Brønsted acid site concentration was determined by measuring Py-IR with a *Thermo Nicolet 5700* FT-IR spectrometer at a resolution of 4 cm<sup>-1</sup>. The catalyst was pelleted into a thin wafer and activated at 450°C (heating rate = 10°C min<sup>-1</sup>) for one hour in vacuum (ca. 10<sup>-6</sup> mbar). After cooling down to 150°C, the apparatus was filled with pyridine until the sample was fully saturated and subsequently equilibrated for one hour. Next, the system was outgassed for one hour to remove physically adsorbed pyridine and a spectrum with the chemisorbed pyridine was collected. Finally, the system was heated again to 450°C (heating rate = 10°C min<sup>-1</sup>) for one hour in vacuum to desorb the pyridine. The concentration of the Brønsted (1540 cm<sup>-1</sup>) acid sites was quantitatively calculated by using a molar integral extinction coefficients of 0.73 cm μmol<sup>-1</sup>.

**Raman spectroscopy:** The Raman spectra of the catalysts were acquired by a *Via Reflex Raman System* which comprises a research grade optical microscope (*Leica DM2700M*, Magnification 5x, 20x, 50x) coupled to a high-performance Raman spectrometer (*Renishaw*) and a 532 nm diode laser as excitation source (*RL532C*, Class 3B).

**X-ray powder diffraction (XRD):** XRD measurements were performed on a *PANalytical Empyrean* diffractometer equipped with a Cu-Kα radiation of λ = 1.54 Å operating at 45 kV and 40 mA. The scanning range was 5 – 70° 2θ with a step size of 0.017°. For the analysis of the diffractograms as well as the

determination of the monoclinic and tetragonal phases, the *PANalytical Highscore Plus* software was used.

### Catalytic measurements

All reactions were performed in an autoclave (300 mL) from *Parr Instruments Co.* (type: *PST FS*, material: HASTELLOY C) with a temperature and stirring controlling device (*Parr Instruments Co. 4848 Reactor Controller*). The liquid samples were analyzed by a gas chromatography (GC) system (*Agilent Technologies 7890B GC*, *HP-5* capillary column (30 m, 0.32 mm inner diameter, 0.25 μm film), equipped with a flame ionization detector (FID) and a mass spectrometer (MS) (*Agilent Technologies 5977 MS*). Data was analyzed with *MassHunter Workstation Software, Qualitative Analysis, Version B.06.00, Agilent Technologies (2012)*.

The reactant and the catalyst were dissolved in 100 mL decalin. After purging the reactor two times with H<sub>2</sub> or N<sub>2</sub>, the pressure was set to 6 bar and heated to the desired temperature with a heating rate of 10°C per minute without stirring. 10°C below the reaction temperature, the total pressure was adjusted and as soon as the target temperature was reached, the stirring rate was set to 700 rpm to start the experiment. During the reaction, in situ sampling was applied. The reaction conditions included a high hydrogen pressure in order to be consistent with the experiments investigating the hydrodeoxygenation of microalgae.

The weight normalized dehydration rate was independent of the employed catalyst amount (ESI,† Fig. S15) and refers to the initial rates which were determined by plotting the conversion of octadecanol versus the reaction time. The slope of the linear fit at low conversions (< 20%) is then multiplied with the initial molar amount of octadecanol and divided by the mass of the catalyst.

### Conflicts of interest

There are no conflicts to declare.

### Acknowledgements

This work was funded by the Alpines AlgenKerosin (FKZ LaBay89A) project by the Bavarian State Ministry for Economic Affairs, Regional Development and Energy and the Bavarian State Ministry of Science and the Arts.

J. A. L. was supported by the U.S. Department of Energy (DOE), Office of Science, Office of Basic Energy Sciences (BES), Division of Chemical Sciences, Geosciences and Biosciences (Transdisciplinary Approaches to Realize Novel Catalytic Pathways to Energy Carriers, FWP 47319). Special gratitude is expressed to A. Brenig and A. Mühlbach for their help in performing experiments.

### References

1. M. Hino and K. Arata, *J. Chem. Soc., Chem. Commun.*, 1988, 1259-1260.

2. J. G. Santiesteban, J. C. Vartuli, S. Han, R. D. Bastian and C. D. Chang, *J. Catal.*, 1997, **168**, 431-441.
3. N. Soultanidis, W. Zhou, A. C. Psarras, A. J. Gonzalez, E. F. Iliopoulou, C. J. Kiely, I. E. Wachs and M. S. Wong, *J. Am. Chem. Soc.*, 2010, **132**, 13462-13471.
4. M. Kantcheva, M. Milanova and S. Mametsheripov, *Catal. Today*, 2012, **191**, 12-19.
5. C. D. Baertsch, K. T. Komala, Y.-H. Chua and E. Iglesia, *J. Catal.*, 2002, **205**, 44-57.
6. J. Macht, C. D. Baertsch, M. May-Lozano, S. L. Soled, Y. Wang and E. Iglesia, *J. Catal.*, 2004, **227**, 479-491.
7. E. I. Ross-Medgaarden, W. V. Knowles, T. Kim, M. S. Wong, W. Zhou, C. J. Kiely and I. E. Wachs, *J. Catal.*, 2008, **256**, 108-125.
8. W. Zhou, E. I. Ross-Medgaarden, W. V. Knowles, M. S. Wong, I. E. Wachs and C. J. Kiely, *Nature Chem.*, 2009, **1**, 722-728.
9. W. Zhou, N. Soultanidis, H. Xu, M. S. Wong, M. Neurock, C. J. Kiely and I. E. Wachs, *ACS Catalysis*, 2017, **7**, 2181-2198.
10. J.-H. Lee, C.-H. Shin and Y.-W. Suh, *Molecular Catal.*, 2017, **438**, 272-279.
11. D. H. Piva, R. H. Piva, C. A. Pereira, D. S. A. Silva, O. R. K. Montedo, M. R. Morelli and E. A. Urquieta-González, *Mater. Today Chem.*, 2020, **18**, 100367.
12. D. G. Barton, M. Shtein, R. D. Wilson, S. L. Soled and E. Iglesia, *J. Phys. Chem. B*, 1999, **103**, 630-640.
13. N. Pfriem, Y. Liu, F. Zahn, H. Shi, G. L. Haller and J. A. Lercher, *J. Am. Chem. Soc.*, 2021, **143**, 20133-20143.
14. V. Lebarbier, G. Clet and M. Houalla, *J. Phys. Chem. B*, 2006, **110**, 13905-13911.
15. F. Gonell, D. Portehault, B. Julián-López, K. Vallé, C. Sanchez and A. Corma, *Catal. Sci. Technol.*, 2016, **6**, 8257-8267.
16. D. G. Barton, S. L. Soled, G. D. Meitzner, G. A. Fuentes and E. Iglesia, *J. Catal.*, 1999, **181**, 57-72.
17. F. Di Gregorio and V. Keller, *J. Catal.*, 2004, **225**, 45-55.
18. I. A. Guschina and J. L. Harwood, in *Algae for Biofuels and Energy*, eds. M. A. Borowitzka and N. R. Moheimani, Springer Netherlands, Dordrecht, 2013, pp. 17-36.
19. C. Zhao, T. Brück and J. Lercher, *Green Chem.*, 2013, **15**.
20. M. Haas and K. Wagner, *Eur. J. Lipid Sci. Technol.*, 2011, **113**, 1219-1229.
21. B. Peng, Y. Yao, C. Zhao and J. A. Lercher, *Angew. Chem. Int. Ed.*, 2012, **51**, 2072-2075.
22. B. Peng, X. Yuan, C. Zhao and J. A. Lercher, *J. Am. Chem. Soc.*, 2012, **134**, 9400-9405.
23. L. Jiménez-Díaz, A. Caballero, N. Pérez-Hernández and A. Segura, *Microb. Biotechnol.*, 2017, **10**, 103-124.
24. M. Scheithauer, R. K. Grasselli and H. Knözinger, *Langmuir*, 1998, **14**, 3019-3029.
25. M. Scheithauer, T. K. Cheung, R. E. Jentoft, R. K. Grasselli, B. C. Gates and H. Knözinger, *J. Catal.*, 1998, **180**, 1-13.
26. D. G. Barton, S. L. Soled and E. Iglesia, *Top. Catal.*, 1998, **6**, 87-99.
27. E. I. Ross-Medgaarden and I. E. Wachs, *J. Phys. Chem. C*, 2007, **111**, 15089-15099.
28. D. S. Kim, M. Ostromecki and I. E. Wachs, *J. Mol. Catal. A: Chem.*, 1996, **106**, 93-102.
29. T. Kim, A. Burrows, C. J. Kiely and I. E. Wachs, *J. Catal.*, 2007, **246**, 370-381.
30. I. E. Wachs, *Catal. Today*, 1996, **27**, 437-455.
31. V. G. Keramidas and W. B. White, *J. Am. Ceram. Soc.*, 1974, **57**, 22-24.
32. E. C. Subbarao, *Zirconia - an overview*, 1981.
33. C. D. Baertsch, S. L. Soled and E. Iglesia, *J. Phys. Chem. B*, 2001, **105**, 1320-1330.
34. J. Macht, R. T. Carr and E. Iglesia, *J. Catal.*, 2009, **264**, 54-66.
35. K.-H. Jacob, E. Knözinger and S. Benier, *J. Mater. Chem.*, 1993, **3**, 651-657.
36. C. Denk, S. Foraita, L. Kovarik, K. Stoerzinger, Y. Liu, E. Baráth and J. A. Lercher, *Catal. Sci. Technol.*, 2019, **9**, 2620-2629.
37. S. Foraita, J. L. Fulton, Z. A. Chase, A. Vjunov, P. Xu, E. Baráth, D. M. Camaioni, C. Zhao and J. A. Lercher, *Chem. Eur. J.*, 2015, **21**, 2423-2434.
38. S. Foraita, Y. Liu, G. L. Haller, E. Baráth, C. Zhao and J. A. Lercher, *ChemCatChem*, 2017, **9**, 195-203.